

A Practical Approach to Generating First-Order Rician Channel Statistics in a RC plus CATR Chamber at mmWave

A. Antón Ruiz, *Student Member, IEEE*, S. Hosseinzadegan *Member, IEEE*, J. Kvarnstrand, *Member, IEEE*, K. Arvidsson, and A. Alayón Glazunov, *Senior Member, IEEE*

Abstract—This paper explores a novel hybrid configuration integrating a Reverberation Chamber (RC) with a Compact Antenna Test Range (CATR) to achieve a controllable Rician K-factor. The focus is testing directive antennas in the lower FR2 frequency bands (24.25-29.5 GHz) for 5G and beyond wireless applications. The study meticulously evaluates 39 unique configurations, using a stationary horn antenna for consistent reference K-factor characterization, and considers variables like absorbers and CATR polarization. Results demonstrate that the K-factor can be effectively adjusted within the hybrid setup, maintaining substantial margins above the noise level across all configurations. Sample independence is confirmed for at least 600 samples in all cases. The Bootstrap Anderson-Darling goodness-of-fit test verifies that the data align with Rician or Rayleigh distributions. Analysis of total received power, stirred and unstirred power and frequency-dependent modeling reveals that power variables are inversely related to frequency, while the K-factor remains frequency-independent. The hybrid RC-CATR system achieves a wide range of frequency-averaged K-factors from -9.2 dB to 40.8 dB, with an average granularity of 1.3 dB. Notably, configurations using co-polarized CATR signals yield large K-factors, reduced system losses, and improved frequency stability, underscoring the system's efficacy for millimeter-wave over-the-air testing. This research offers a cost-efficient and repeatable method for generating complex Rician fading channels at mmWave frequencies, crucial for the effective OTA testing of advanced wireless devices.

Index Terms—Compact Antenna Test Range (CATR), mmWave, Over-the-air (OTA) testing, Reverberation Chamber, Rician K-factor

I. INTRODUCTION

Over-The-Air (OTA) testing is now the standard for verifying the radiated communication performance of wireless

devices, including smartphones, tablets, access points, base stations, and vehicle-mounted wireless equipment [1], [2]. It provides a realistic performance assessment in a controlled and repeatable environment. It is crucial for testing fully integrated devices and active antenna systems with multiple elements without any connectors [3].

Wireless devices operate in complex and diverse propagation channels, but for practical and cost-effective OTA measurements, testing should focus on a subset of relevant scenarios. The spatial characteristics of propagation channels and their interaction with antennas influence the variability in communication link quality [4]. The Power-Angle Spectrum (PAS), which describes the Angle of Arrival (AoA) distribution of waves incident on the device, affects the fading distribution of the received signal at the Device Under Test (DUT). The Rician fading channel model, defined by a deterministic Line-Of-Sight (LOS) component and a random Non-Line-Of-Sight (NLOS) component, characterizes this interaction, with the envelope of the received signal following the Rician Probability Distribution Function (PDF) [5]. The K -factor, representing the ratio of LOS to NLOS power, defines the model, with $K = 0$ indicating a Rayleigh PDF and $K \rightarrow \infty$ representing a deterministic, non-fading component.

Millimeter Wave (mmWave) technology is crucial for Fifth Generation (5G) due to its large bandwidth availability, though it exhibits higher path loss and sparser, more directional channels compared to sub-10 GHz frequencies [6], [7]. Consequently, higher K -factors are more common. To overcome path loss, 5G systems employ massive Multiple-Input Multiple-Output (MIMO) arrays with highly directive antennas, which must be tested in various channel conditions to emulate different Rician K -factors.

There are two limiting propagation scenarios: Rich Isotropic Multipath (RIMP) and Random Line-Of-Sight (Random-LOS). The RIMP scenario represents an isotropic AoA distribution, modeling the random propagation component. In contrast, the Random-LOS scenario depicts a Dirac-delta PAS, where deterministic waves impinge on the DUT from specific orientations. RIMP can be reproduced in a Reverberation Chamber (RC), and Random-LOS in anechoic or semi-anechoic chambers, given proper design [8]–[10]. A new testing setup incorporating a Compact Antenna Test Range (CATR) system within an RC allows for the emulation of these complex scenarios, with Rician fading with various K -factors [11], [12].

Manuscript submitted for review on February 28, 2024. The work of Alejandro Antón is supported by the European Union's Horizon 2020 Marie Skłodowska-Curie grant agreement No. 955629. Andrés Alayón Glazunov also kindly acknowledges funding from the ELLIIT strategic research environment (<https://elliit.se/>).

A. Antón Ruiz is with the Radio Systems Group, within the Department of Electrical Engineering, University of Twente, Enschede, The Netherlands (e-mail: a.antonruiz@utwente.nl).

S. Hosseinzadegan is with the Electromagnetic Compatibility (EMC) team, Volvo Technology AB, Gothenburg, Sweden (e-mail: samar.hosseinzadegan@volvo.com).

J. Kvarnstrand is with the Method and Development Groups, Bluetest AB, Gothenburg, Sweden (e-mail: john.kvarnstrand@bluetest.se).

K. Arvidsson is with Bluetest AB, Gothenburg, Sweden (e-mail: klas.arvidsson@bluetest.se).

A. Alayón Glazunov is with the Department of Science and Technology, Linköping University, Nörrköping Campus, Sweden (e-mail: andres.alayon.glazunov@liu.se). He is also affiliated with the Department of Electrical Engineering, University of Twente, Enschede, The Netherlands.

Extensive research has been conducted on characterizing the K -factor in RCs, aiming to achieve a low K -factor for accurate RIMP emulation, which reduces uncertainty in RC measurements like Total Radiated Power (TRP) [13]–[18].

Emulating Rician channels with variable K -factors in RCs is not new. Previous studies have explored various methods to control K -factors across different conditions and frequencies, typically up to 6 GHz [19]–[25]. However, these methods often involve post-processing or physical adjustments that are not ideal for active device testing and can lead to mechanical and repeatability challenges. Additionally, there is limited work validating that the resulting data follows a Rician distribution, a critical aspect for meaningful K -factor estimation.

Our approach uses a CATR to generate a Plane Wave (PW), which ensures compliance with far-field requirements even for large DUTs and when high K -factors are desired. This setup includes a LOS blocking plate between the RIMP antenna and the DUT, allowing for controlled LOS components and lower K -factors in hybrid RC and CATR modes. This configuration ensures the DUT experiences a consistent LOS component within the 30 cm “quiet zone” of the CATR. We also strategically place absorbers to manage power from the CATR, enhancing repeatability and control over K -factor variations, especially when the DUT is mounted on a roll tower, offering a significant improvement over previous methods [24].

To the authors’ best knowledge, this is the first time a mixed RC plus CATR OTA setup is thoroughly investigated regarding the realization of a wide range of Rician K -factors at the mmWave frequencies. The contributions of this paper can be summarized as follows:

- We study in more depth the mixed RC plus CATR OTA setup proposed in [12] as a means to produce a Resonating Cavity Hybrid Anechoic-Reverberation Chamber (RC-HARC) to generate complex Rician fading channels at mmWave frequencies by mixing the contributions of the two available channel modes, Pure-LOS produced by the CATR and the RIMP produced by the RIMP Measurement Antenna (RIMPMA). This is a cost-efficient solution because the RC-HARC is implemented as an already existing, commercially available product in a way that it was not originally designed for, without needing relevant modifications. This work analyzes not only the K -factor frequency response as in [12], but also the average and frequency response of the unstirred, stirred, and total received powers, as well as the Signal to Noise Ratio (SNR).
- We provide a substantial analysis of different configurations of the RC-HARC at the lower FR2 bands for 5G, i.e., from 24.25 – 29.5 GHz, achieving a wide range of frequency-averaged K -factors, from -9.2 to 40.8 dB, with a dB-averaged granularity of 1.3 dB, being of 5.1 dB in the worst case. We regard the generation of environments with a wide range of K -factors, including large ones, as highly relevant for mmWave OTA testing.
- We consider the use of absorbers designed to attenuate the reflections coming from the CATR, as well as attenuators and the two different polarizations of the CATR feeder, to generate channels with different K -factors.

All these elements are introduced in a controlled way in the setup, minimizing repeatability issues. In particular, the absorbers have a fixed mount in the chamber, and the CATR polarization change is implemented via a switch.

- We propose a horn antenna as a reference for mmWave measurements K -factor. We do this partly based on the recommendations of 3GPP [26] guidelines in other areas, where it is specified to use a reference antenna that excites the RC similarly to the one of the DUT. e.g., for the spatial uniformity test. At mmWave, antennas are expected to have directive radiation patterns and, consequently, high gains [6]. This is heavily DUT-dependant, e.g. a base station will have a much larger gain than a mobile phone. For the proposed setup, the gain has a larger impact on the achieved K -factor when the CATR excitation is used. Therefore, since directive antennas are used at mmWave but their gain is not fixed, we decide to use a Reference Horn Antenna (RHA) with around 14 dBi gain [27] at the considered frequencies. This antenna is similar to one of the antennas used in [6] to conduct urban propagation measurements at 28 GHz, which is also a horn antenna with 15 dBi gain, supporting the reasonability of our choice.
- We follow a similar approach to what the Cellular Telephone Industries Association (CTIA) [28] proposes for the assessment of uncertainties due to the lack of spatial uniformity of the RC. [28] requires a series of precharacterization measurements of the RC which result in an uncertainty figure for each loading condition of the chamber. This information is stored in a table and used accordingly when taking measurements. The precharacterization measurements must be repeated only when substantial modifications are made to the chamber. In our case, we propose a precharacterization measurements assessment of the reference K -factor value for each of the 39 considered configurations. The idea is to take these measurements once, store them, and select the proper configuration to obtain the desired environment, i.e., the desired K -factor perceived by the RHA in the same position as it was taken during the precharacterization measurements.
- We check the acquired samples for independence, which is required to use the estimator from [20], as well as for the proper application of the Goodness-of-Fit (GoF) tests.
- We check that the acquired data follows a Rician distribution, making the K -factor evaluation meaningful. We use a bootstrap-based Anderson-Darling (AD) GoF test, which is the best way found in the literature to check for GoF for Rician distribution without prior knowledge of the distribution’s parameters. In addition, it is used to check for GoF for Rayleigh distribution. To the authors’ best knowledge, this is the first time it is applied to statistical data obtained from RC measurements.

The remainder of the paper is organized as follows: Section II presents the setup for the experiments, presenting the RC-HARC chamber, the RHA, the considered configurations of the chamber, as well as the connections of the different

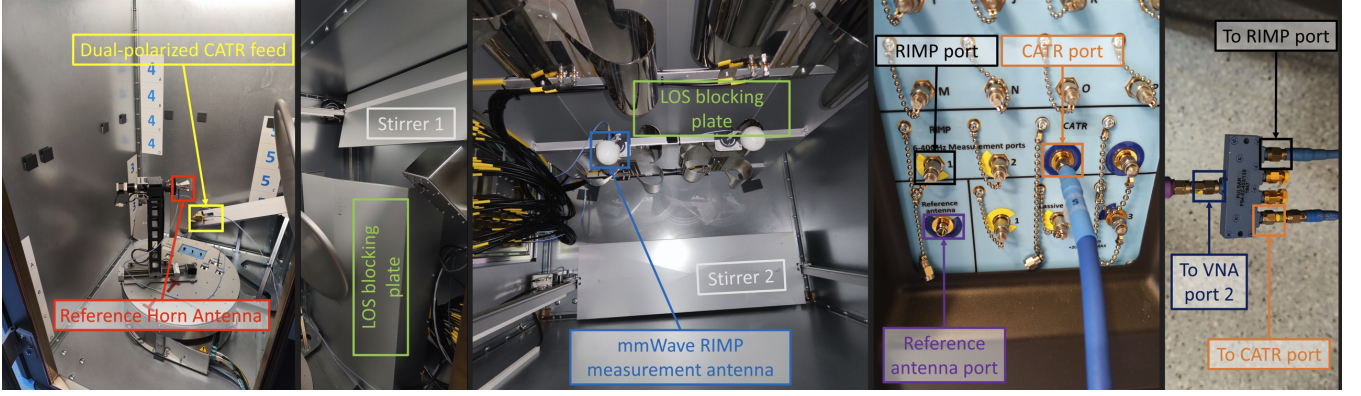


Fig. 1. From left to right, Blueptest RTS65 with the CATR option and without any absorbers installed, corresponding to the “NoAs” case, depicting the RHA and the dual-polarized CATR feed. Then we have the Stirrer 1 and the LOS blocking plate, which hides the mmWave RIMPMA, depicted in the next picture, which is a ceiling shot taken from behind the LOS blocking plate, where the Stirrer 2 can be seen. Then, we have the front panel of the RC, with the three used ports highlighted: RIMP port, CATR port, and reference antenna port. Finally, the 1:4 splitter goes outside the chamber and indicates where each port is connected. Note the terminations in the unused ports. Note also that the splitter configuration shown is for the RaC case. In R and C cases the port of the splitter going to the CATR or RIMP ports, respectively, would be terminated too.

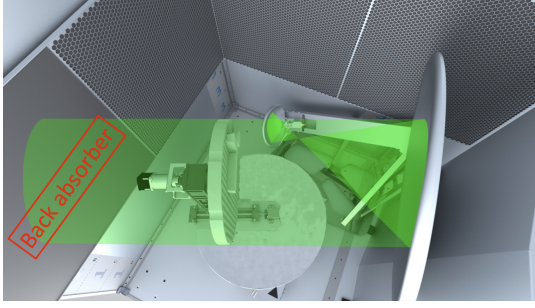


Fig. 2. CAD render showing geometry and signal flow (in green). The “quiet zone” is located within the lightest green volume. Notice how all absorbers are installed in the chamber, corresponding to the “AAs” case, including the back absorber, depicted in red, which intercepts the signal flow. Source: [11].

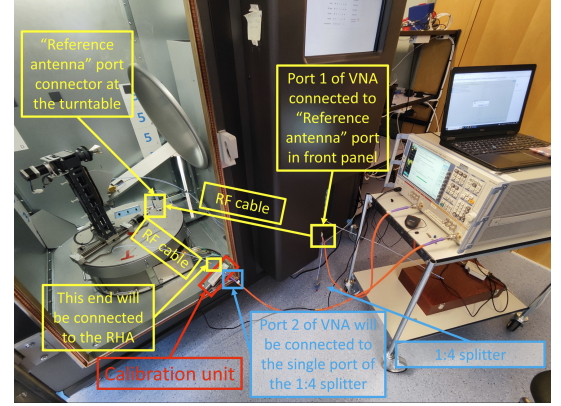


Fig. 3. Experiment setup for calibrating the VNA.

cables and ports and the Vector Network Analyzer (VNA) configuration. Section III presents the methodology used for the analysis of the measured data, including the assumed Rician distributed signal model, the method used to check for the independence of the samples, the procedure to obtain the estimate of the received power from S_{21} data, the SNR estimation method, the chosen K -factor estimator, and the AD bootstrap-based GoF test used. Section IV presents the results based on the methodology described in Section III, therefore presenting the independence of samples, average SNR and power, K -factor, including its frequency dependence, and the results of the GoF tests. Finally, Section V presents the conclusions after analyzing the results from Section IV, as well as the limitations and future work.

II. EXPERIMENTAL SETUP AND MEASUREMENT CASES

This section describes the measurement setup to generate the RIMP, the Pure-LOS, and the compound propagation channel.

A. RC-HARC Chamber

Fig. 1 shows the experimental setup showing the interior of a Blueptest RTS65 RC chamber with the CATR option installed, with dimensions of the chamber of $1945 \times 2000 \times 1440$ mm³ (WxHxD) [11]. The chamber is designed to be used as a compact 2-in-1 test system, providing either a RIMP or a Pure-LOS only field in the test zone when it is excited through the RIMP or the CATR port, respectively. Hence, TRP and radiation pattern measurements can be performed within the same space since the CATR mode uses absorbers on the walls. For the RIMP operation, the chamber has a total of 3 physical stirring mechanisms. One of them is the turntable, which is not used in this work. The other two stirrers, which are linear, are shown in Fig. 1 as Stirrer 1 and Stirrer 2. They operate as just one stirring mechanism, moving coordinately.

The CATR generates a PW with a dual parabolic reflector illuminated by a dual-polarized antenna feed shown in yellow in Fig. 1, and it has a 0.6 dB amplitude and a 4° phase ripples. The performance is maintained from 24.25 – 42 GHz within a 30 cm diameter cylindrical “quiet zone” shown in Fig. 2 [29]. It must be noted that the alignment between the DUT and the CATR will have a relevant effect on the realized

K -factor, while the position of the DUT, as long as it is within the “quiet zone”, will have a smaller impact since the direct coupling between the CATR and a DUT pointing at it has a small variation within the “quiet zone”. The polarization of the feeder antenna of the CATR can be selected using a passive switch or connecting to the other CATR port.

The reflections coming from the reflector or the DUT are reduced by carbon-loaded foam absorbers placed around the chamber, as shown in Fig. 2. Except for the absorber on the wall towards which the PW is directed (“back absorber”), all the other absorbers are Frequency Selective Absorber (FSA). They are covered by a metallic honeycomb pattern with a size of the periodic metallic pattern such that it is small compared to the wavelength at sub-6 GHz frequencies for which the chamber is also designed to operate in RIMP, thus providing a strong reflection. However, at mmWave, the periodic metallic pattern size is larger than the wavelength. Therefore providing a small reflection and letting the signals reach the carbon-loaded absorber behind the honeycomb. The back absorber has the same material and size as the FSA, except that the metallic honeycomb part is removed, thus providing less reflection. This is because most of the power coming from the reflector is directed to this back absorber.

B. Considered Measurement Configurations

A total of 39 measurement cases were considered, by combining 4 configuration variables in the setup specified below.

- RC, CATR or mixed mode of the RC-HARC chamber are used. As depicted in Fig.1, we use the RIMP and CATR ports of the chamber to excite either the RIMPMA or the dual-polarized CATR feed, respectively. The first will emulate the RIMP environment, generating multiple PWs. The second will emulate the Pure-LOS environment (a single PW), only in case of installing all the absorbers. If not, it will generate an environment with a direct PW and then some reflections that might or might not interact with the stirrers. Both ports can be used simultaneously using a splitter as shown in Fig. 1. Therefore, the possible configurations are:
 - R - only RIMP port connected to the splitter to generate the RIMP channel.
 - C - only CATR port connected to the splitter to emulate a Pure-LOS channel when all absorbers are placed or a Rician channel.
 - RaC - RIMP and CATR ports connected to the splitter. A mixture of stirred and unstirred components produces a Rician channel with desired K -factors.
- CATR dual-polarized feeder. The feeder has two orthogonal polarizations that can be selected using a passive switch that routes the signal to each feeder port. A single polarization is used at a time in our work.
 - PSX - is stated in RIMP only cases in which the position of the passive switch is irrelevant since the CATR port is not used.
 - PS1 - passive switch in position 1 corresponding to the co-polarized field component of the RHA in the exper-

iment’s setup. This produces a strong LOS coupling of the CATR signal to the RHA.

- PS2 - passive switch in position 2 corresponding to the cross-polarized to the RHA in the experiment’s setup. This produces a weak LOS coupling of the CATR signal to the RHA.

■ Absorbers are used in three configurations.

- NoAs - no absorbers with minimal attenuation of both RIMP and CATR signals.
- BAs - back absorber only, as shown in Fig. 1, with a large reduction of the stirred component coming from the reflections of the CATR signal.
- AAs - all absorbers present, as shown in Fig. 3, with a large reduction of the stirred component in general.

■ Attenuators are used in the cases where RIMP and CATR ports are used at the same time (i.e., the “RaC” cases). The attenuators allow changing the realized K -factor, with minimal changes to the setup. The adapters (2.92 mm male to 2.4 mm female and 2.4 mm male to 2.92 mm female) are required for the “X0ATR” configurations but not for the “X0ATC” cases due to the used components and arrangement of ports of the chamber. More on this can be found in Section II-C1.

- NAT - no attenuators.
- 10ATC - 10 dB attenuator on CATR branch.
- 20ATC - 20 dB attenuator on CATR branch.
- 10ATR - 10 dB attenuator plus adapters on RIMP branch.
- 20ATR - 20 dB attenuator plus adapters on RIMP branch.

An exhaustive list of the cases can be found in Table I, where each case has been assigned to a numeric identifier, which will be used in the figures to ease interpretation.

C. Instruments and Measurements

1) *Cabling*: To perform this experiment, a 2.92 mm 1:4 splitter was used. The VNA has 1.85 mm ports, to which 2.4 mm cables are connected directly. The cable connected to port 2 of the VNA is connected to the single port of the splitter with a 2.4 mm female to 2.92 mm male adapter. For the “R” cases, three of the ports of the splitter are terminated, and the other is connected via a 2.92 mm cable to the “RIMP” port of the chamber (2.92 mm) that reaches the RIMPMA. For the “C” cases, three of the splitter ports are terminated. The other port is connected via a 2.92 mm male to 2.4 mm female adapter and a 2.4 mm cable to the “CATR” port of the chamber (1.85 mm), that reaches the dual-polarized CATR feed. The “RC” cases are a mixture of “R” and “C”, where the splitter is set up as depicted in Fig. 1. Then the port 1 of the VNA is connected to the “Reference antenna” port of the chamber, that reaches the “Reference antenna” port at the turntable, which is then connected to the RHA via a 2.4 mm cable.

2) *VNA and Measurement Configuration*: The VNA was configured to perform an S_{21} frequency sweep from 24.25 – 29.5 GHz with 10 MHz steps according to the FR2 bands resulting in 526 Frequency Samples (FS) for each of the 39 cases. An Intermediate Frequency (IF) bandwidth of 1 KHz

TABLE I
RELEVANT STATISTICS OF K -FACTOR, STIRRED, UNSTIRRED AND TOTAL POWERS.

Column	1	2	3	4	5	6	7	8	9	10	11	12	13	14	15	16
Case	Identifier	$\langle K \rangle_{FS}$ [dB]	K CV	K DR [dB]	$\langle \Omega \rangle_{FS}$ [dBm]	Ω CV	Ω DR [dB]	$\langle P_s \rangle_{FS}$ [dBm]	P_s CV	P_s DR [dB]	$\langle P_d \rangle_{FS}$ [dBm]	P_d CV	P_d DR [dB]	GoF PR Rayleigh	GoF PR Rician	$\langle SNR \rangle_{FS}$ [dB]
NoAs_R_PSX	1	-9.2	1.0	38.7	-68.8	0.4	6.9	-69.3	0.4	5.9	-78.5	1.1	37.3	92.4%	89.2%	27.4
BA_s_R_PSX	2	-7.6	1.0	35.3	-71.6	0.4	8.2	-72.3	0.4	6.4	-79.9	1.2	36.4	89.5%	88.2%	24.6
AA_s_R_PSX	3	-5.5	1.1	31.7	-76.0	0.5	9.2	-77.2	0.4	6.6	-82.5	1.3	34.8	81.6%	88.6%	20.2
NoAs_C_PS1	4	20.7	0.2	4.6	-53.3	0.4	8.3	-74.1	0.3	5.8	-53.4	0.4	8.3	0.0%	95.1%	42.9
BA_s_C_PS1	5	35.0	0.1	2.8	-53.4	0.4	6.3	-88.4	0.4	6.8	-53.4	0.4	6.3	0.0%	94.5%	42.8
AA_s_C_PS1	6	40.8	0.2	3.6	-53.4	0.4	6.2	-94.2	0.4	6.4	-53.4	0.4	6.2	0.0%	94.7%	42.9
NoAs_C_PS2	7	-2.6	1.0	38.4	-72.5	0.4	9.3	-74.3	0.3	5.7	-77.2	1.0	38.2	63.9%	93.5%	23.8
BA_s_C_PS2	8	6.0	1.0	39.8	-81.7	0.9	17.5	-88.4	0.4	6.6	-82.8	1.1	39.6	14.4%	96.8%	14.6
AA_s_C_PS2	9	11.5	1.0	37.7	-82.8	1.0	20.5	-94.2	0.4	6.3	-83.1	1.1	36.0	7.8%	95.2%	13.7
NoAs_RaC_PS1	10	14.7	0.2	4.7	-53.2	0.4	8.6	-68.1	0.4	5.6	-53.4	0.4	8.8	0.0%	96.6%	43.0
NoAs_RaC_PS1_10ATC	11	6.0	0.3	8.0	-62.2	0.4	9.3	-69.2	0.4	6.0	-63.1	0.5	10.6	0.0%	94.7%	34.1
NoAs_RaC_PS1_20ATC	12	-2.9	0.6	30.6	-67.5	0.4	8.2	-69.3	0.4	6.2	-72.2	0.8	28.5	62.9%	92.6%	28.7
NoAs_RaC_PS1_10ATR	13	19.6	0.2	4.5	-53.4	0.4	8.2	-73.0	0.3	6.3	-53.4	0.4	8.3	0.0%	95.8%	42.9
NoAs_RaC_PS1_20ATR	14	20.6	0.2	4.4	-53.4	0.4	8.2	-74.0	0.3	5.9	-53.4	0.4	8.2	0.0%	94.5%	42.9
BA_s_RaC_PS1	15	18.8	0.1	3.2	-53.4	0.4	7.1	-72.2	0.4	6.3	-53.4	0.4	7.2	0.0%	96.4%	42.9
BA_s_RaC_PS1_10ATC	16	9.1	0.2	6.2	-62.7	0.4	9.4	-72.3	0.4	6.3	-63.2	0.4	10.0	0.0%	95.4%	33.5
BA_s_RaC_PS1_20ATC	17	-0.2	0.6	23.2	-69.4	0.5	9.9	-72.3	0.4	6.3	-72.5	0.7	25.7	31.2%	95.4%	26.8
BA_s_RaC_PS1_10ATR	18	28.1	0.1	2.6	-53.4	0.4	6.2	-81.5	0.4	6.4	-53.4	0.4	6.2	0.0%	95.6%	42.8
BA_s_RaC_PS1_20ATR	19	33.6	0.1	2.8	-53.4	0.4	6.2	-87.0	0.4	7.0	-53.4	0.4	6.2	0.0%	95.1%	42.8
AA_s_RaC_PS1	20	23.8	0.1	3.0	-53.4	0.4	6.5	-77.1	0.4	6.6	-53.4	0.4	6.5	0.0%	94.3%	42.9
AA_s_RaC_PS1_10ATC	21	14.0	0.2	5.4	-63.0	0.4	8.0	-77.2	0.4	6.5	-63.2	0.4	8.1	0.0%	95.8%	33.2
AA_s_RaC_PS1_20ATC	22	4.4	0.4	16.6	-71.4	0.5	12.0	-77.2	0.4	6.6	-72.7	0.6	19.0	1.9%	94.9%	24.8
AA_s_RaC_PS1_10ATR	23	33.2	0.1	3.0	-53.4	0.4	6.2	-86.5	0.4	7.1	-53.4	0.4	6.2	0.0%	94.5%	42.8
AA_s_RaC_PS1_20ATR	24	39.0	0.1	3.3	-53.4	0.4	6.3	-92.4	0.4	6.4	-53.4	0.4	6.3	0.0%	95.2%	42.8
NoAs_RaC_PS2	25	-6.7	1.0	31.2	-67.3	0.4	7.6	-68.1	0.4	5.9	-75.0	1.1	34.1	87.5%	89.0%	28.9
NoAs_RaC_PS2_10ATC	26	-8.8	0.9	36.6	-68.6	0.4	6.7	-69.2	0.4	6.0	-78.1	1.0	35.0	91.6%	87.3%	27.6
NoAs_RaC_PS2_20ATC	27	-9.2	1.0	37.5	-68.8	0.4	6.8	-69.3	0.4	6.1	-78.5	1.1	40.4	92.6%	88.6%	27.4
NoAs_RaC_PS2_10ATR	28	-3.4	1.0	33.4	-71.6	0.4	8.9	-73.2	0.3	5.7	-76.8	1.0	35.8	70.9%	93.2%	24.7
NoAs_RaC_PS2_20ATR	29	-2.7	1.0	36.8	-72.4	0.4	9.5	-74.2	0.3	5.6	-77.1	1.0	35.0	65.4%	92.4%	23.9
BA_s_RaC_PS2	30	-5.9	0.9	47.6	-71.3	0.4	7.7	-72.2	0.4	6.3	-78.3	1.0	46.1	84.4%	91.4%	25.0
BA_s_RaC_PS2_10ATC	31	-7.5	1.0	31.4	-71.6	0.4	7.7	-72.3	0.4	6.2	-79.9	1.1	33.8	90.5%	88.2%	24.6
BA_s_RaC_PS2_20ATC	32	-7.6	1.0	39.4	-71.6	0.4	8.2	-72.3	0.4	6.3	-80.0	1.2	38.3	91.1%	88.4%	24.6
BA_s_RaC_PS2_10ATR	33	-0.2	1.0	51.2	-78.7	0.6	11.4	-81.5	0.4	6.3	-82.0	1.1	53.6	48.1%	94.9%	17.6
BA_s_RaC_PS2_20ATR	34	4.7	1.0	40.6	-81.3	0.8	16.0	-87.0	0.4	6.6	-82.6	1.1	43.2	19.2%	95.4%	15.1
AA_s_RaC_PS2	35	-2.4	1.0	31.6	-75.2	0.5	9.6	-77.1	0.4	6.7	-79.7	1.0	33.0	60.8%	92.2%	21.1
AA_s_RaC_PS2_10ATC	36	-5.0	1.0	39.4	-76.0	0.5	9.8	-77.2	0.4	6.6	-82.1	1.2	42.7	77.9%	90.9%	20.3
AA_s_RaC_PS2_20ATC	37	-5.4	1.1	39.6	-76.1	0.5	9.6	-77.2	0.4	6.6	-82.4	1.3	42.8	79.8%	90.5%	20.2
AA_s_RaC_PS2_10ATR	38	4.1	1.1	43.5	-81.2	0.8	15.7	-86.6	0.4	6.6	-82.8	1.2	42.5	24.0%	95.1%	15.2
AA_s_RaC_PS2_20ATR	39	9.8	1.0	41.9	-82.7	1.0	19.6	-92.6	0.4	5.9	-83.1	1.1	43.7	8.9%	94.7%	13.8

was used, which provides a noise level below -82 dBm according to the manufacturer. The output power of the VNA was set to 10 dBm. The VNA calibration plane was, on the one side, at the port of the RHA and, on the other side, at the 2.4 mm female port of the adapter connected to the single port of the 1:4 splitter. This is depicted in more detail in Fig. 3.

For each FS, 600 samples were collected. The samples were taken at 600 unique positions of the two mode-stirrers of the chamber (see Fig. 1) while keeping the turntable fixed during all measurements to ensure that the RHA was pointed towards the reflector. Each of the 600 positions of the stirrers is the same for all frequencies since the movement of the stirrers is done in the outer loop, being the frequency sweep in the inner loop.

D. Reference Antenna

All measurements have been done with a linearly-polarized double ridged horn antenna, designed to operate from 4.5 – 50 GHz, whose specs can be found in [27]. The RHA is always placed statically (see Fig. 1), such that the turntable will not rotate. Hence, the turntable stirring is off. The chosen position aligns the max gain of the RHA and its polarization with the CATR; hence both the co- or cross-polarization can be measured. This serves our purposes well because a more controlled interaction between the RHA and the CATR can be achieved, thus achieving large K -factors. The horn antenna

has been chosen for reference measurements because it's a directional antenna with a well-known pattern and accessible Radio Frequency (RF) ports, allowing complex-valued S_{21} measurements. K -factor can then be straightforwardly estimated as discussed further in Section III-A.

III. ANALYSIS METHODOLOGY

This section presents the assumed Rician fading PDF and the corresponding parameters to emulate the first-order statistics in the RC-HARC. We present the method to determine the number of independent samples and estimate the SNR, the average received power Ω , and the K -factor. The GoF test used to determine whether the generated signals belong to the Rician PDF is also presented.

A. Rician Signal Model

The Rician distribution of the envelope of the complex signal amplitude received by the antenna $|v|$ is given by [5],

$$f_{|v|}(|v|) = \frac{2(1+K)|v|}{\Omega} \exp\left(-K - \frac{(K+1)|v|^2}{\Omega}\right) \times I_0\left(2\sqrt{\frac{K(1+K)}{\Omega}}|v|\right), \quad (1)$$

where $v = S_{21}$ is, in our case, the measured quantity in the chamber, and I_0 is the modified Bessel function of the first

kind and zeroth order. The PDF parameters are the Rician K -factor defined as

$$K = \frac{P_d}{P_s}, \quad (2)$$

where P_d and P_s are the powers of the LOS and the RIMP components, respectively. More specifically, we are considering P_d as all the power that does not interact with the mode stirrers of the chamber. On the other hand, P_s is the power that interacts with the chamber's stirrers, and we will assume that results from an isotropic wave field distribution, thus generating a RIMP field. The K -factor measures the severity of field fluctuations generated for a specific scenario. The second parameter is the total received power

$$\Omega = P_d + P_s, \quad (3)$$

i.e., the average received power. The two limiting cases, the RIMP and the Pure-LOS channels, directly arise from $K \rightarrow 0$ and $K \rightarrow \infty$, respectively. The former turns into the Rayleigh PDF [8], [24], while the latter case turns into the Dirac- δ function [5]. Intermediate values of K will describe Rician propagation channels between the RIMP and the LOS channels.

B. Independence of the samples

The independence of the samples is relevant for several aspects of this work, including the GoF tests and the K -factor estimation. Following the discussion in [30], [31], the number of independent or effective samples N_{eff} in the presence of more than one mode stirrer should be computed through the use of a circular-shift correlation matrix. The threshold used in [30], [31] for considering the correlation between samples is consistent with the one present in the standards [26], [32]. If fully satisfied, it ensures, with a 95% likelihood and for sample sizes larger than 100, that all samples are independent. In the case of this work, there are two mode stirrers, although they move at the same time at equispaced steps. N_{eff} is evaluated according to (3) from [30], where $N = 600$ are samples corresponding to unique positions of the mode stirrers and measured for each of the 526 FS.

C. Received Power Estimation

As discussed in Section II-C2, the VNA was configured to perform a frequency sweep reporting the calibrated complex-valued S_{21} . To assess the SNR, it is necessary to know the measured power of the receiving port of the VNA for each sample and the actual noise level of the instrument at the receiving port.

To determine the actual measured power at the VNA receiving port, we accounted for all compensated losses and measured them along with the output power of the VNA port. Consequently, the received power at the VNA port is calculated as follows.

$$P_{\text{rec}}[\text{dBm}] = P_{\text{out}}[\text{dBm}] - L_{\text{cal}}[\text{dB}] - L_{\text{eff}}[\text{dB}] + S_{21}[\text{dB}], \quad (4)$$

where the notation used indicates that the variable $X[\text{dB}]$ denotes the dB value of the variable X in linear units.

Furthermore, the meaning of the terms in (4) is explained below.

- $L_{\text{cal}}[\text{dB}]$ denotes the total losses of all the cables and connectors accounted for in the calibration (see Fig. 3).
- $L_{\text{eff}}[\text{dB}]$ denotes the losses of the reference antenna due to its efficiency, which are compensated by measurement software.
- $P_{\text{out}}[\text{dBm}]$ is set to 10 dBm, which, according to the calibration report of the instrument, can be output for the considered frequency range. Therefore, we use 10 dBm across all the frequency ranges.
- $S_{21}[\text{dB}] = 20 \log_{10} |S_{21}|$ is the link (receive) power between the transmit and receive port in the absence of the rest of considered losses and VNA output power.

Hence, an estimate of the total (average) received power at a single frequency is estimated by

$$\hat{\Omega} = \langle P_{\text{rec}} \rangle_{\text{SP}}, \quad (5)$$

where P_{rec} is the received power (4) in linear units [mW], and the brackets $\langle \bullet \rangle_{\text{SP}}$ denote sample averaging over the N_{eff} stirrer positions (SP).

D. SNR Estimation

The noise level of the VNA $NL[\text{dBm}]$ was estimated for each 526 FS. The measurement was conducted by terminating both VNA ports with 50 Ω loads and then measuring the S_{21} with the same IF bandwidth of 1 kHz and an output power of 0 dBm. Hence, with calibration turned off, the measured $|S_{21}|^2$ in dB is equivalent to a noise realization's power level in dBm. For each of the 526 FS, 1000 samples of S_{21} (noise realizations) were collected, with a sampling time spacing of 10 ms. Then, the noise level at a given frequency was determined as the average of those 1000 noise samples (NS), i.e., $\langle |S_{21}|^2 \rangle_{\text{NS}}$. Each FS single noise level value is denoted as $NL[\text{dBm}] = 10 \log(\langle |S_{21}|^2 \rangle_{\text{NS}})$. The average noise level of the VNA over the considered frequency range from 24.25 – 29.5 GHz with this configuration is $\langle NL \rangle_{\text{FS}}[\text{dBm}] = -96.3$ dBm, which is below the -82 dBm that the instrument manufacturer guarantees. The peak-to-peak variation of $NL[\text{dBm}]$ is 4.1 dB.

With the average received power and the noise level, the SNR at stirrer position $i_{\text{SP}} \in [1, 600]$ and FS $i_{\text{FS}} \in [1, 526]$ can be computed as

$$\text{SNR}(i_{\text{SP}}, i_{\text{FS}})[\text{dB}] = P_{\text{rec}}(i_{\text{SP}}, i_{\text{FS}})[\text{dBm}] - NL(i_{\text{FS}})[\text{dBm}]. \quad (6)$$

It must be noted that (6) can be less than 0 if two conditions are met: first, if $S_{21}[\text{dB}]$ is as low that $P_{\text{rec}}[\text{dBm}]$ is dominated by the noise level, i.e., if $S_{21}[\text{dB}] \rightarrow -\infty$ and, second, if the noise realization for that particular SP sample i_{SP} and at a particular FS i_{FS} is below the average noise level at that FS. Therefore, looking at the average SNR rather than the sample by sample SNR is more relevant. Hence $\text{SNR}_{\text{avg}}[\text{dB}]$ is defined as the average SNR in dB of a given configuration

$$\text{SNR}_{\text{avg}}[\text{dB}] = \langle \langle P_{\text{rec}} \rangle_{\text{SP}} \rangle_{\text{FS}}[\text{dBm}] - \langle NL \rangle_{\text{FS}}[\text{dBm}], \quad (7)$$

where the operators $\langle \bullet \rangle_{\text{SP}}$ and $\langle \bullet \rangle_{\text{FS}}$ denote sample averaging over the stirrer positions (SP) and frequency samples (FS),

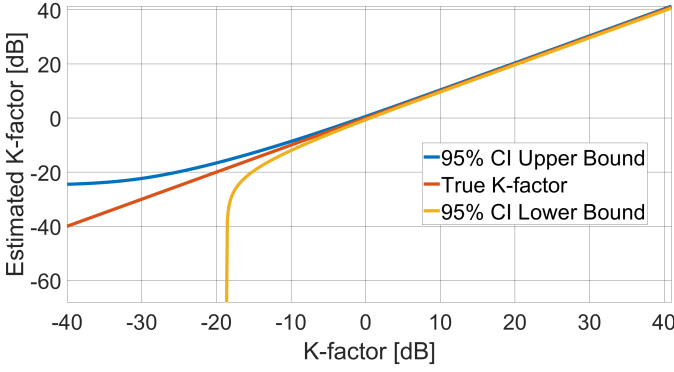


Fig. 4. 95% CI for the K -factor estimator used in this work (from [20]) and 600 samples or stirrers' positions.

respectively. The averaging is applied to the linear values, not the ones in dB.

E. K -factor Estimation

We use the K -factor estimator presented in [20] because it is unbiased, which, for the sake of completeness, we reproduce here

$$\hat{K} = \frac{N_{\text{eff}} - 2}{N_{\text{eff}} - 1} \hat{K}_2 - \frac{1}{N_{\text{eff}}}, \quad (8)$$

$$\hat{K}_2 = \frac{|\langle \tilde{S}_{21} \rangle_{\text{SP}}|^2}{\langle |\tilde{S}_{21}|^2 \rangle_{\text{SP}} - |\langle \tilde{S}_{21} \rangle_{\text{SP}}|^2}, \quad (9)$$

where

$$\tilde{S}_{21} = S_{21} \sqrt{\frac{\hat{\Omega}}{\langle |S_{21}|^2 \rangle_{\text{SP}}}}, \quad (10)$$

is the normalized transfer function, N_{eff} is the number of independent samples, which will be proven to be equal to the number of stirrers' positions (600) in Section IV-A. In [33], it was observed that due to its unbiased nature, it could lead to negative (in linear units) estimates of low K -factors when the number of samples is limited. In our case, we have $N_{\text{eff}} = 600$, which makes the 95% CI hit an asymptote on its lower bound when the actual K -factor is lower than, approximately, -18 dB, as can be observed in Fig. 4. In this work, for the FS of each case where the estimated K -factor is negative (in linear units), we disregard that FS of that case from all the analysis of the considered parameters (Ω, K, P_s and P_d). The percentage of FS where the estimated K -factor is negative is 0.3% on average across all cases and, for an individual case, the highest percentage of FS where the estimated K -factor is negative is 1.3%. The expressions to obtain the 95% CI are (43) and (44) from [20].

F. Goodness-of-Fit Testing

GoF tests assess whether a given dataset comes from a hypothesized distribution. This work considers two separate null hypotheses: whether the data follows Rayleigh PDF, while the second is whether the data follows the Rician PDF. This type of GoF problem is a composite one or, equivalently, H_0 is composite. The alternative hypothesis H_1 is that the

distribution followed by the data belongs to a different family than the one specified by H_0 . For the so-called type I error, i.e., the likelihood of incorrectly rejecting H_0 , $\alpha = 0.05$ is set, meaning that the GoF test has a 5% likelihood of rejecting H_0 when it is true. On the other hand, for the so-called type II error, i.e., failing to reject H_0 when it is false, the likelihood of the event is β . The power of the test is defined as $1 - \beta$. Ideally, α and β shall be as close to 0 as possible. However, that is not possible due to the finite nature of the number of independent samples. Indeed, α and β are inversely related, so, for example, decreasing α would increase β , thus decreasing the power of the test, and vice versa. The power of the test can only be computed when H_1 is specified [34], which is not the case in this work, and testing it for an array of relevant distributions falls beyond the scope of the work.

The data obtained here is continuous, so the chi-square GoF would be disregarded. However, according to [34], a modified version of the chi-square test can be applied to continuous data with generally good performance. Nevertheless, the performance of the AD test is generally better than the chi-square test, according to their results. In addition, the AD GoF test has been successfully used for RC applications [35], and therefore we use it.

Now moving to the composite H_0 , it must be noted that, if one recklessly applies a GoF test applicable to a simple H_0 in the case of a composite H_0 , it will lead to an increased probability of accepting H_0 [35], or, similarly, a decrease of the power of the test. This would make the test useless since it will not reject H_0 when it is false as much as one would expect from the power of the test for simple H_0 . To solve this, there are tables of modified critical values for some GoF tests. However, while there are tables of critical values for the composite GoF test when H_0 is that the distribution is an exponential [36] (or Rayleigh, for which the same values apply [35]), there are not, to the best of the authors' knowledge, for the case of the Rician distribution. For these cases, resorting to bootstrap-based GoF tests is necessary [37].

Hence, a bootstrap-based AD GoF test with α set to 0.05 is used in this work. H_0 is set to be either a Rayleigh or a Rician distribution, i.e., two different GoF tests are applied for every of the 526 FS that contain 600 samples for each of the 39 considered configurations. The data used as input for each of the GoF tests is composed of the 600 samples of a given FS and a given configuration (e.g., "BAs_RaC_PS1"). The implementation of the bootstrap method is based on a modification of the "adtest" function from MATLAB to use it for Rayleigh and Rician distributions with composite H_0 . The original "adtest" function lacks the possibility of being used as a GoF test for Rayleigh and Rician distributions, so we have introduced the necessary changes and new code to make it work for such distributions. This function contains the function "adtestMC", which we also modify and it simulates the critical values and p-values for the AD test using a Monte Carlo simulation. Instead of setting a fixed number of bootstrap samples ("B" from [37]), it sets them to make the standard error of the estimated p-value lower than the parameter "mctol", which we set to 0.01, being this the default value of "mctol", which is present in the original "adtestMC"

function.

IV. RESULTS AND ANALYSIS

In this section, we present the results of the parameters specified in Section III.

A. Independence of the samples

Applying the methodology from Section III-B, we found that all the collected samples can be considered independent. Namely, $N_{\text{eff}} = N = 600$, i.e., all collected samples are independent for all considered chamber configurations and frequencies.

B. SNR

The frequency-averaged SNR or $\langle \text{SNR} \rangle_{\text{FS}}$ is at least 13.7 dB and up to 43 dB, as shown in column 16 of Table I. This is a good margin to the average noise floor; therefore, this, together with the sample independence, leads us to assume that all the measured samples can be used in our analysis. This does not mean that they are noise-free. Indeed, if we consider the SNR at a particular frequency, there are some cases in which the average $\langle \text{SNR} \rangle_{\text{SP}}$ is rather low. For example, as low as 1.11 dB for a FS of case 9. However, this is a limited occurrence, since, e.g., the percentage of frequencies at which the SNR is 5 dB or more, is only less than 100% for cases 9 (89%) and 39 (95%). Moreover, the percentage of frequencies at which the SNR is 10 dB or more, is only less than 100% for cases 8 (83%), 9 (65%), 34 (93%), 38 (94%) and 39 (66%).

C. Received Power

For example, for case 1, where an average K -factor of -9.28 dB is achieved, the losses from the tip of the 1:4 splitter to the RHA are around 56 dB. Again, this might be suitable for some applications. While for others, such for example, trying to test a device in high SNR scenarios, it is not. This and other aspects should be investigated in the future, looking towards the practical challenges of OTA testing. The received power or Ω [dBm] statistics are presented in columns 5–7 in Table I. It can be observed that the frequency-averaged received power $\langle \Omega \rangle_{\text{FS}}$ is higher for cases in which the CATR is excited in co-polarization with the RHA ("PS1", or cases 4–6 and 10–24). In fact, in the "PS1" cases without attenuators in the CATR branch, the $\langle \Omega \rangle_{\text{FS}}$ remains almost unchanged. This is because the direct-LOS component is dominating, which can be observed in the high values of $\langle K \rangle_{\text{FS}}$ (column 2), which results in a relatively strong $\langle P_d \rangle_{\text{FS}}$ (column 11) and relatively weak $\langle P_s \rangle_{\text{FS}}$ (column 8). Therefore, adding a RIMP component by exciting the RIMP port or changing the absorber configuration does not have a noticeable effect on $\langle \Omega \rangle_{\text{FS}}$. The system losses of the CATR system when no polarization discrimination is applied, i.e. when there is co-polarization ("PS1"), are much lower than those of the RC excitation ("R"), which was expected, since usually a LOS scenario is going to be less lossy than a NLOS one. On the other hand, "PS2" cases have significantly lower $\langle \Omega \rangle_{\text{FS}}$ than their matching "PS1" cases and, in addition, the "C" "PS2" cases (7–9) have a

lower $\langle \Omega \rangle_{\text{FS}}$ than the "R" cases (1–3) while having the latter a lower $\langle K \rangle_{\text{FS}}$ (column 2). As for the addition of absorbers, "PS1" cases without attenuation are almost not affected, while "PS2" cases are affected more (larger $\langle \Omega \rangle_{\text{FS}}$ decrease) in the transition from "NoAs" to "BAs" than in the transition from "BAs" to "AAs". As expected, the back absorber attenuates most of the CATR power. Meanwhile, "R" cases suffer a larger $\langle \Omega \rangle_{\text{FS}}$ decrease when going from "BAs" to "AAs" than when going from "NoAs" to "BAs". This is because the losses for the RIMP component are impacted by chamber loading, which is increased considerably more in the case of going from "BAs" to "AAs" (1 absorber to 6 absorbers) than when going from "NoAs" to "BAs" (0 absorbers to 1 absorber).

Now moving to Fig. 5a, it can be observed that below the $\langle \Omega \rangle_{\text{FS}}$ of case 37 of -76 dB, there is a high increase in the Ω Coefficient of Variation (CV), which reaches 1 for the lowest $\langle \Omega \rangle_{\text{FS}}$ cases. Above that, there is a mild trend to a decreased Ω CV with higher $\langle \Omega \rangle_{\text{FS}}$, until reaching a floor at around 0.4. The behavior of Ω CV resembles an exponential decay with increasing $\langle \Omega \rangle_{\text{FS}}$ values. It is worth noting that the behavior of Ω CV "PS1" is different to that of "PS2" and "R", needing a higher $\langle \Omega \rangle_{\text{FS}}$ to achieve a Ω CV as low as the one of "PS2" and "R". The same trends apply to Ω Dynamic Range (DR), being worth noting that there are some high $\langle \Omega \rangle_{\text{FS}}$ cases of "PS1" that exhibit different Ω DR for approximately the same $\langle \Omega \rangle_{\text{FS}}$.

D. K-factor

The frequency-averaged K -factors or $\langle K \rangle_{\text{FS}}$ results are shown in columns 2–4 from Table I. As seen, $\langle K \rangle_{\text{FS}}$ covers a wide range from -9.2 to 40.8 dB. The two extreme values correspond to cases 1 (RC excitation only and no absorbers) and case 6 (CATR excitation only in co-polarization with the RHA and with all absorbers), respectively. One relevant aspect that can be observed is that the cases of either RC excitation only and those in which the CATR is excited (only or along with RIMP) in the cross-polarization of the RHA ("PS2"), generally yield low $\langle K \rangle_{\text{FS}}$. Conversely, the cases in which the CATR is excited (only or along with RIMP) in the co-polarization of the RHA ("PS1"), yield higher $\langle K \rangle_{\text{FS}}$. The intervals of $\langle K \rangle_{\text{FS}}$ produced by the RC excitation only and CATR excitation only in the co-polarization of the RHA ("PS1"), for each of the absorber configurations, are $[-9.2, 20.7]$ dB for the case with no absorbers ("NoAs"), $[-7.6, 35]$ dB for the cases with the back absorber ("BAs"), and $[-5.5, 40.8]$ dB for the cases with all absorbers ("AAs"). These intervals contain all the $\langle K \rangle_{\text{FS}}$ of the rest of the cases. Moreover, the interval of $\langle K \rangle_{\text{FS}}$ of the "BAs" cases is fully overlapped with the intervals of $\langle K \rangle_{\text{FS}}$ of the "NoAs" and "AAs" cases.

In Fig. 5b, it can be observed that the frequency variations heavily depend on the excitation of the system. For RC excitation only and all cases in which the CATR is excited in cross-polarization with the RHA ("PS2"), both the CV and the DR are far superior to those of the cases where the CATR is excited in co-polarization with the RHA ("PS1"). It is relevant to note that, for similar $\langle K \rangle_{\text{FS}}$ values, the

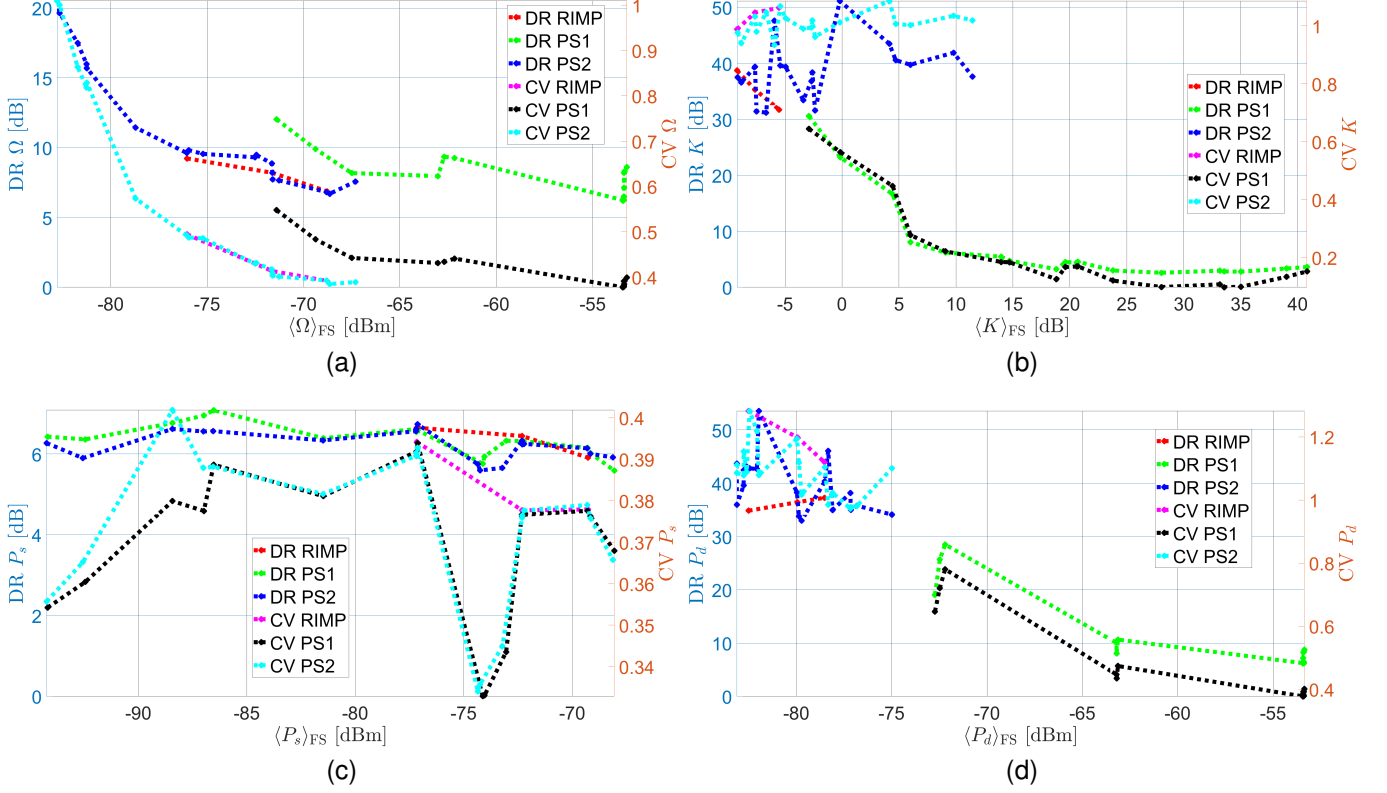


Fig. 5. DR and CV of Ω , K , P_s and P_d . Split into cases in which only RIMP is excited (red and magenta), cases in which the CATR is excited, along or not with RIMP, co-polarized with the RHA or “PS1” (green and black), and cases in which the CATR is excited, along or not with RIMP, cross-polarized with the RHA or “PS2” (blue and cyan). The purpose of these plots is to help identify trends in terms of DR and CV of Ω , K , P_s and P_d depending on the frequency-averaged values of Ω , K , P_s and P_d , respectively. The split between “RIMP”, “PS1” and “PS2” cases is made because they showed different behaviors among them while being similar for the cases they comprise, i.e., “PS1” cases behave in a relatively consistent manner, which is different to how “RIMP” and “PS2” behave.

use of the co-polarized CATR signal provides a much more frequency-stable K -factor than using the CATR in cross-polarization. As for the RC excitation only, it performs, at similar $\langle K \rangle_{FS}$ values, quite similarly to the CATR in cross-polarization regarding frequency stability. Finally, there is a trend in the case of the co-polarized CATR of decreasing frequency variations with increasing $\langle K \rangle_{FS}$, although it is not completely monotonic. On the one hand, this behavior is expected because the estimator has a narrower CI for higher $\langle K \rangle_{FS}$. On the other hand, this behavior might also be explained because of the direct coupling between the CATR signal and the RHA, which dominates when $\langle K \rangle_{FS}$ is high, is more stable with the frequency than the stirred and other unstirred paths which are not the LOS itself.

Fig. 6 shows all the cases sorted in increasing order of the frequency-averaged K -factor. The 39 measured cases offer a granularity of the K -factor control of 1.3 dB on average from -9.2 dB to 40.8 dB. However, there are some large increments of up to 5.1 dB going from case 18 to case 23, as shown in Fig. 6. All other transitions are rather smooth.

E. Stirred Power

The stirred power or P_s [dBm] statistics are presented in columns 8 – 10 from Table I. It can be observed that the frequency-averaged stirred power $\langle P_s \rangle_{FS}$ is higher for

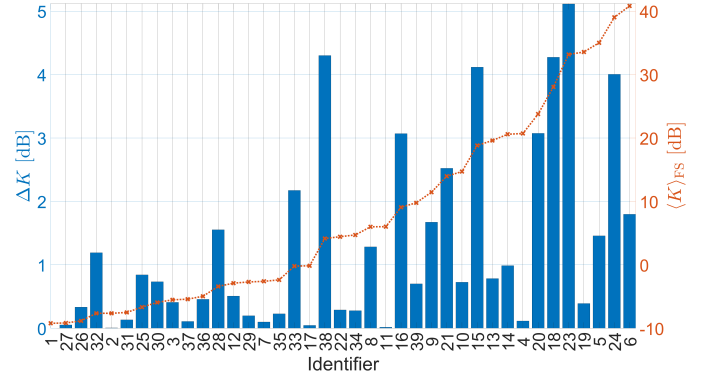


Fig. 6. Sorted K -factors and increments between them.

the cases where no absorbers are used, decreasing as more absorbers are added. It must be noted that all “PS1” and “PS2” cases, including the ones with CATR excitation only, behave in a very similar manner in terms of $\langle P_s \rangle_{FS}$, P_s CV and P_s DR (see Fig. 5c). This is relevant, since it indicates that the stirred components produced by the CATR mostly impinge in the RHA with polarization balance or, at least, that the stirrers make the polarizations impinge similarly the RHA on average when the RHA is in that orientation. Furthermore, in the “RaC” cases without RC branch attenuators, P_s is dominated

by the contribution from the RC excitation. Moreover, the “C” cases and the “RaC” “x0ATR” cases suffer very large decreases in $\langle P_s \rangle_{FS}$ when the back absorber is placed, being the decrease milder when adding the rest of the absorbers. This, as already shown in Section IV-C, implies that most of the CATR power which is not directly coupled with the RHA is captured by the back absorber. For the “R” cases, it works the other way around due to the larger increase of chamber load when adding the rest of the absorbers compared to adding just the back absorber. It is also worth noting that, for some of the “AAs” cases, in particular, 6, 9, 24, and 39, the $\langle P_s \rangle_{FS}$ is very close to the average $\langle NL \rangle_{FS}$ [dBm] of -96.3 dBm. This could impact the estimated K -factor for those cases, since the actual $\langle P_s \rangle_{FS}$ might be lower than what is shown here, but the noise floor of the VNA limits how low it can be. Finally, there are not any identifiable trends in P_s CV and P_s DR for $\langle P_s \rangle_{FS}$, aside from having a relatively low range of CV and DR values (see the scales of CV and DR for the rest of plots from Fig. 5), i.e., all considered cases perform in a more similar way than in the case of the rest of analyzed parameters.

F. Unstirred Power

The unstirred power or P_d [dBm] statistics are presented in columns 11 – 13 in Table I. The frequency-averaged stirred power $\langle P_d \rangle_{FS}$ is higher for the “PS1” cases, where the P_d contribution is dominated by the direct coupling between the RHA and the CATR, since no relevant changes in $\langle P_d \rangle_{FS}$ are observed when changing the absorber configurations, which has an impact on the unstirred components that are not the direct coupling. This is observed even for the “20ATC” cases. However, in these some differences start to appear when changing absorber configurations. For “PS2” cases, either for “RaC” “x0ATR” and “C” cases, it is observed that the reduction in $\langle P_d \rangle_{FS}$ when going from “NoAs” to “BAs” configurations is much larger (around 5 dB) than when going from “BAs” to “AAs”. This means that, in these “NoAs” cases, the contribution to P_d through the CATR excitation in cross-pol to the RHA is dominated by the unstirred multipath components, which are strongly attenuated when the back absorber is placed.

From Fig. 5d, it can be highlighted that, unlike for the rest of the analyzed parameters, there is a gap between the achieved $\langle P_d \rangle_{FS}$ values of “PS1” cases, and those from “PS2” and “R” cases. This is due to the strong coupling between the CATR and the RHA for “PS1” cases, which, even with 20 dB attenuators provide larger $\langle P_d \rangle_{FS}$ values than any of the “PS2” and “R” cases. As for P_d CV and P_d DR, there is some tendency to decrease for both of them with increasing values of $\langle P_d \rangle_{FS}$.

G. Goodness-of-fit test

The GoF tests at each FS of every of the 39 cases are applied to the 600 samples, which, as we already established in Section IV-A, are independent for all cases.

In Table I, the Pass Rate (PR) of the bootstrap-based AD GoF tests with α set to 0.05 is displayed in columns 14 and

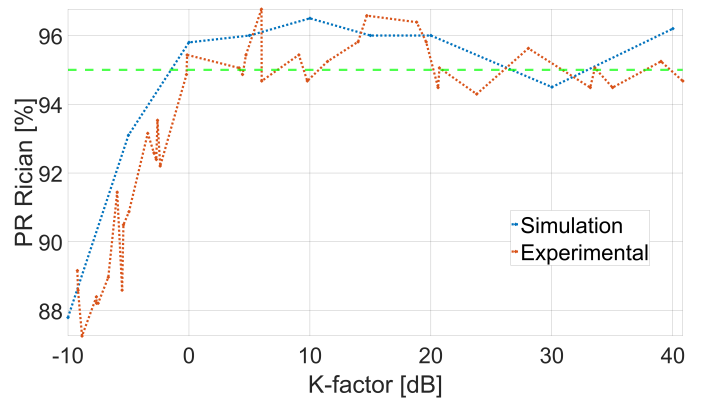


Fig. 7. Bootstrap AD GoF test for Rician distribution versus K -factor from measurements and simulations. The green line is set at the expected 95% PR. Note that the K -factor in the x-axis corresponds to $\langle K \rangle_{FS}$ for the experimental results.

15. This PR is defined as the number of FS where the GoF test could not reject the null hypothesis H_0 divided by the total number of FS. H_0 is the data that comes from a Rician distribution in one case; in the other, H_0 is the data that comes from a Rayleigh distribution.

Since α is set to 0.05, the expected PR if the data comes from a distribution of the family of H_0 , i.e., if H_0 is true, would be 95%. Therefore, the expected PR for the GoF test with H_0 being that the data comes from a Rician distribution, is 95%, since we expect to get a signal that is Rician distributed in all cases. However, the results are not completely aligned with the expectations. In some cases, we get close to the expected 95% PR, but in other cases, we get lower ones, being the minimum 87.3%. In particular, it can be observed that there appears to be some correlation between lower $\langle K \rangle_{FS}$ and lower PRs for Rician distribution as the H_0 . This can be observed in Fig. 7, where simulations have also been included to confirm if the observed behavior of the experimental data is expected or not. The simulations consisted of generating 1000 random samples with a size of 600 samples from a Rician distribution with a fixed K -factor. Then, the same bootstrap-based AD GoF test for H_0 being that the distribution of the data is Rician was applied to each of the 1000 sets of 600 samples, obtaining a 1000 rejections or not of H_0 . From that, the PR was computed as the percentage of not rejection of H_0 . This was repeated for as many fixed K -factors as points are in the simulations curve (9). Although the underlying reasons for the observed behavior of the PR of the GoF test w.r.t. the K -factor should be further studied and tackled, which we consider falling beyond the scope of this work, the fact that we observe very similar behavior for the experimental data leads us to the conclusion that the experimental data for each of the considered cases follows a Rician distribution. Thus, the consideration of K -factor, Ω , P_s , and P_d as fundamental parameters to describe our experimental data is appropriate.

On the other hand, we observe an inverse relation between K -factor and PR for the AD GoF test with H_0 being that the data comes from a Rayleigh distribution. This is something to be expected, i.e., a Rayleigh distribution is a Rician distribution with a K -factor equal to 0 or $-\infty$ dB, so

TABLE II
FITTING PARAMETERS AND R^2 OF K , Ω , P_s , AND P_d .

Column	1	2	3	4	5	6	7	8	9	10	11	12	13
Case	Identifier	A_K	n_K	R_K^2	A_Ω	n_Ω	R_Ω^2	A_s	n_s	R_s^2	A_d	n_d	R_d^2
NoAs_R_PXS	1	-11.6	0.9	0.2%	-69.3	-6.4	90.4%	-69.8	-6.5	97.0%	-82.4	-5.6	5.8%
BA_s_R_PXS	2	-10.1	0.2	0.0%	-72.1	-6.3	82.2%	-72.8	-6.4	95.0%	-82.9	-6.2	7.1%
AA_s_R_PXS	3	-8.1	-0.7	0.1%	-76.7	-6.9	74.6%	-77.7	-6.6	94.1%	-85.7	-7.3	10.0%
NoAs_C_PS1	4	20.6	-0.7	5.8%	-53.9	-6.5	83.3%	-74.5	-5.8	96.2%	-53.9	-6.5	83.1%
BA_s_C_PS1	5	35.0	-0.1	0.6%	-53.9	-6.6	96.0%	-88.9	-6.5	96.3%	-53.9	-6.6	96.0%
AA_s_C_PS1	6	40.7	-0.7	6.0%	-53.9	-6.6	96.4%	-94.6	-5.9	91.2%	-53.9	-6.6	96.4%
NoAs_C_PS2	7	-5.1	0.7	0.1%	-73.1	-5.2	47.3%	-74.7	-5.8	95.1%	-79.8	-5.1	4.9%
BA_s_C_PS2	8	3.5	4.4	3.7%	-83.1	-4.5	11.3%	-89.0	-6.9	96.6%	-85.4	-2.5	1.2%
AA_s_C_PS2	9	8.5	6.2	5.6%	-84.9	-1.7	0.9%	-94.7	-6.2	94.0%	-86.1	0.0	0.0%
NoAs_RaC_PS1	10	14.6	-0.1	0.1%	-53.7	-6.4	80.7%	-68.5	-6.3	97.2%	-53.9	-6.4	79.7%
NoAs_RaC_PS1_10ATC	11	5.8	-0.3	0.3%	-62.8	-6.6	73.6%	-69.6	-6.4	96.9%	-63.8	-6.7	63.9%
NoAs_RaC_PS1_20ATC	12	-4.0	0.2	0.0%	-68.1	-6.4	73.8%	-69.8	-6.4	96.9%	-73.7	-6.2	16.2%
NoAs_RaC_PS1_10ATR	13	19.5	-0.5	3.3%	-53.9	-6.5	83.5%	-73.5	-5.9	96.9%	-53.9	-6.5	83.2%
NoAs_RaC_PS1_20ATR	14	20.5	-0.7	5.4%	-53.9	-6.5	83.4%	-74.4	-5.8	96.4%	-53.9	-6.5	83.2%
BA_s_RaC_PS1	15	18.8	-0.2	0.8%	-53.9	-6.5	92.8%	-72.7	-6.3	94.9%	-53.9	-6.5	92.6%
BA_s_RaC_PS1_10ATC	16	9.0	-0.5	1.3%	-63.3	-6.7	79.5%	-72.8	-6.3	95.0%	-63.8	-6.8	75.7%
BA_s_RaC_PS1_20ATC	17	-1.0	0.1	0.0%	-70.0	-6.3	62.0%	-72.8	-6.3	95.0%	-73.8	-6.2	21.2%
BA_s_RaC_PS1_10ATR	18	28.0	-0.1	0.2%	-53.9	-6.6	95.8%	-82.0	-6.5	96.3%	-53.9	-6.6	95.8%
BA_s_RaC_PS1_20ATR	19	33.5	-0.2	0.9%	-53.9	-6.6	96.0%	-87.5	-6.4	96.3%	-53.9	-6.6	96.0%
AA_s_RaC_PS1	20	23.7	-0.1	0.2%	-53.9	-6.6	94.6%	-77.6	-6.6	94.4%	-53.9	-6.6	94.6%
AA_s_RaC_PS1_10ATC	21	13.9	-0.3	1.1%	-63.6	-6.9	85.9%	-77.7	-6.6	94.4%	-63.8	-6.9	85.0%
AA_s_RaC_PS1_20ATC	22	3.9	-0.2	0.1%	-72.2	-6.8	57.1%	-77.7	-6.6	94.3%	-73.7	-6.8	37.3%
AA_s_RaC_PS1_10ATR	23	33.1	0.0	0.0%	-53.9	-6.6	96.4%	-87.0	-6.6	94.9%	-53.9	-6.6	96.4%
AA_s_RaC_PS1_20ATR	24	39.0	-0.6	5.6%	-53.9	-6.6	96.8%	-92.9	-6.0	92.5%	-53.9	-6.6	96.8%
NoAs_RaC_PS2	25	-9.2	2.6	1.3%	-67.8	-5.9	78.3%	-68.6	-6.3	97.0%	-77.8	-3.7	2.6%
NoAs_RaC_PS2_10ATC	26	-11.0	0.2	1.1%	-69.1	-6.3	89.3%	-69.6	-6.4	96.9%	-80.7	-4.3	4.0%
NoAs_RaC_PS2_20ATC	27	-11.5	0.7	0.1%	-69.3	-6.4	90.1%	-69.8	-6.4	96.8%	-81.3	-5.8	6.5%
NoAs_RaC_PS2_10ATR	28	-5.8	1.4	0.4%	-72.2	-5.5	56.5%	-73.6	-6.0	96.2%	-79.4	-4.6	4.2%
NoAs_RaC_PS2_20ATR	29	-5.2	1.3	0.3%	-73.0	-5.3	48.4%	-74.7	-5.8	95.1%	-79.8	-4.5	3.8%
BA_s_RaC_PS2	30	-8.1	1.7	0.6%	-71.8	-6.1	77.6%	-72.7	-6.4	94.9%	-80.8	-4.6	4.4%
BA_s_RaC_PS2_10ATC	31	-9.7	1.1	0.3%	-72.1	-6.2	82.3%	-72.8	-6.3	95.0%	-82.5	-5.2	5.9%
BA_s_RaC_PS2_20ATC	32	-10.1	1.1	0.3%	-72.1	-6.2	82.2%	-72.8	-6.4	95.0%	-82.9	-5.2	5.2%
BA_s_RaC_PS2_10ATR	33	-2.7	3.2	2.0%	-79.4	-5.5	37.6%	-82.0	-6.5	96.5%	-84.6	-3.3	2.1%
BA_s_RaC_PS2_20ATR	34	2.4	4.3	3.9%	-82.5	-4.5	13.7%	-87.5	-6.7	96.9%	-85.2	-2.4	1.2%
AA_s_RaC_PS2	35	-4.9	2.8	1.4%	-75.9	-6.0	52.8%	-77.6	-6.7	94.4%	-82.6	-3.9	2.7%
AA_s_RaC_PS2_10ATC	36	-7.6	0.5	0.0%	-76.6	-6.6	70.4%	-77.7	-6.6	94.3%	-85.3	-6.1	6.3%
AA_s_RaC_PS2_20ATC	37	-8.1	-0.8	0.1%	-76.7	-6.8	73.1%	-77.7	-6.6	94.3%	-85.8	-7.4	9.1%
AA_s_RaC_PS2_10ATR	38	1.3	4.7	3.5%	-82.5	-4.4	13.1%	-87.1	-6.7	95.8%	-85.7	-2.0	0.7%
AA_s_RaC_PS2_20ATR	39	6.8	5.8	4.7%	-84.6	-2.1	1.6%	-93.0	-6.3	96.2%	-86.2	-0.5	0.0%

the lower the K -factor, the closer the PR should be to 95%. These results show that the considered cases are not achieving a pure Rayleigh distributed signal, although some of them, especially case 1, come close to it. In particular, cases 1, 2, 26, 27, 31 and 32 have a PR for Rayleigh very close to or over 90%, with a maximum $\langle K \rangle_{FS}$ of -7.6 dB. Therefore, although accepting some error, we could approximate cases with $\langle K \rangle_{FS}$ lower than -7.6 dB by a Rayleigh model. On the other hand, the increased rejection (lower PR) of H_0 of Rayleigh distribution when $\langle K \rangle_{FS}$ becomes larger, i.e., the distribution becomes less similar to a Rayleigh, indicates that the applied GoF test is working properly.

On another note, the fact that the lowest achieved $\langle K \rangle_{FS}$ is -9.2 dB (case 1) is because turntable stirring is not being used. As shown in [15], this method effectively reduces $\langle K \rangle_{FS}$. A measurement in the same setup as case 1 but with turntable stirring was performed, obtaining a $\langle K \rangle_{FS}$ of -17.6 dB, thus obtaining a channel much closer to RIMP. Traditional RC measurements such as TRP or antenna efficiency are usually performed with turntable stirring in Bluetest's systems.

H. Frequency dependence of the estimated distribution parameters

In the above sections, we studied the statistics of the generated Rician channels as averaged over frequency or considering their statistics over frequency. In this section, we study their frequency dependence. This is done to understand

whether there are relevant trends that we should note for channel emulation purposes. For that, we produce the following fitting curves

$$K[\text{dB}] = A_K + 10n_K \log_{10}(f/f_0), \quad (11)$$

$$\Omega[\text{dBm}] = A_\Omega + 10n_\Omega \log_{10}(f/f_0), \quad (12)$$

$$P_d[\text{dBm}] = A_d + 10n_d \log_{10}(f/f_0), \quad (13)$$

$$P_s[\text{dBm}] = A_s + 10n_s \log_{10}(f/f_0), \quad (14)$$

where f_0 is set to 27 GHz. The election of f_0 is based on the fact that the considered frequency range of 24.25 – 29.5 GHz contains the n257 and n258 5G FR2 bands, which are commonly referred to as the 28 GHz and 26 GHz bands, respectively, due to their center frequencies. Therefore, we have considered f_0 to be in the middle of the bands' center frequencies: 27 GHz. The parameters for the fitting are A and n . A will be the value of the fitted curve at f_0 , while n will describe the frequency dependence of the fitted data. In particular, n represents the exponent of the frequency for K , Ω , P_s , and P_d expressed in linear units. The fitting results are shown in Table II, including the R^2 value. We will focus on n rather than A , since we are interested in analyzing the frequency dependence of K , Ω , P_s , and P_d . In addition, the frequency plots of K , Ω , P_s , and P_d and the corresponding fitting curves for cases 1, 10, and 25 can be found in Fig. 8. The selection of cases was made to illustrate three different relevant configurations under the same absorber configuration, having RC excitation only in case 1, RC and CATR in co-polarization with the RHA in case 10, and RC and CATR in cross-polarization with the RHA in case 25.

From the presented results, it can be highlighted that both P_s and P_d are inversely related to the frequency for all cases (except case 9, which has no relation between P_d and frequency). This behavior is also observed in [24]. The n_s values are quite similar for all cases. On the other hand, the n_d values have a larger variation, being very similar among "PS1" cases. Since Ω is the sum of P_s and P_d , then it is also inversely related with the frequency in all cases. Although this is not plotted in [24], it is also the case there due to P_s and P_d being inversely related with frequency, so being Ω their sum, it is then also inversely proportional to the frequency. The inverse relation of Ω , P_s , and P_d with the frequency can be observed in Fig. 8 (d-l). In addition, the n_Ω values exhibit the same trend of being stable among "PS1" cases. Conversely, the K -factor does not have a general direct or inverse relation with frequency. It is worth noting that most "PS1" cases have a negative and small n_K , i.e., a slight inverse relation with the frequency (Fig. 8b). In comparison, [24] shows a direct dependence on the frequency of K -factor when both horn antennas are co-polarized, which would be comparable to the "PS1" cases. In our work, as stated above, these cases mostly show a slight inverse relation with frequency. This implies that the inverse relation with the frequency of P_d is larger (more negative) than the one from P_s in our work, i.e. $n_d < n_s$. In [24], it happens that $n_d > n_s$. While we do not go into the reasons why this is different in both works or, more generally, into the frequency dependence modeling of K , Ω , P_s , and P_d , we acknowledge it as a point of future

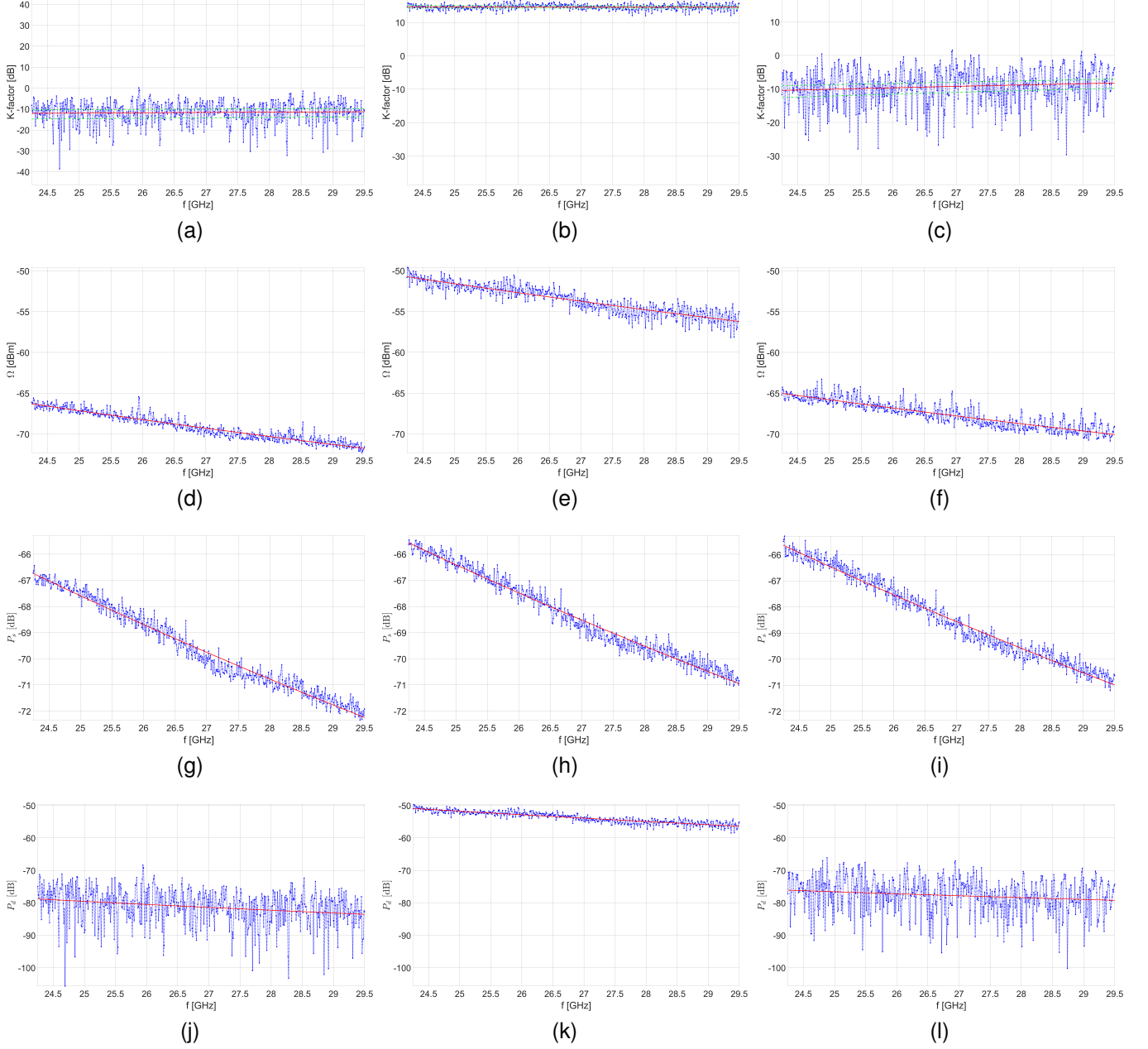


Fig. 8. Frequency plots of K , Ω , P_s and P_d for cases, from left to right, 1, 10, and 25. The estimated values of each parameter are represented in blue. The values coming from the fittings are represented in red. K plots also have two green lines that indicate the 95% CI of the K estimator, computed from (43) and (44) from [20].

work. On the other hand, most “PS2” cases have a positive and generally larger n_K , i.e., a direct relation with the frequency (Fig. 8c). “R” cases show a direct relation with frequency for the “NoAs” (Fig. 8a) and “BAS” cases, but inverse for the “AAs” case. In comparison, we have [14], where a similar RC (RTS chamber) is used in its traditional, no Rician emulation, mode and with different loadings. As can be seen, the K -factor is inversely related to the frequency in all loading conditions, although this inverse relationship seems to weaken as the frequency increases. In our work, we observe a direct relation with frequency for less loaded setups (“NoAs” and “BAS”) and an inverse relation for the heavily loaded scenario (“AAs”). Although we do not focus on the comparison with

[14], we say that the differences in the behavior of K might be explained by the large difference in considered frequencies, which, for example, change which component dominates the quality factor of the chamber Q , as stated in [38].

On the other hand, the R^2 value for P_s is very high for all cases, which implies that the proposed fitting curves explain almost all the variability of P_s with the frequency. In the case of P_d , the R^2 values are high for the “PS1” cases and low for the “R” and “PS2” ones. This is because “PS1” cases (Fig. 8k) have a P_d mostly contributed by the direct coupling of the RHA and the CATR, while in the “R” and “PS2” cases, P_d is mostly contributed by a sum of reflections that do not interact with the stirrers. Such a sum can have large variations

due to phase changes of different reflections' path lengths, resulting in constructive or destructive interference. Therefore, it is somewhat expected to observe variations that cannot be approximated by a smooth fitting curve, being this reflected in the much lower R^2 values for the fitting of P_d for "R" (Fig. 8j) and "PS2" (Fig. 8l) cases. Since, again, Ω is the sum of P_s and P_d , the R^2 values of Ω are a result of a weighted combination of the variability of P_s and P_d that can and cannot be explained by the proposed models. Therefore, since all P_s have high R^2 values, the limiting factor is P_d . Hence, the R^2 values of Ω are high when either P_s is larger than P_d (low K) or when the case is a "PS1" one, since the R^2 of P_d will be high. Conversely, the R^2 values of Ω are low when P_s is smaller than P_d (high K) and, at the same time, the case is a "PS2" one, since the R^2 of P_d will be low. Finally, the R^2 values of K are low in all cases, which implies that most variability of K w.r.t. the frequency cannot be explained by the fitted model.

On another note, in Fig. 8 (a-c), the 95% CI of the K -factor estimator has been plotted for the fitted model. The goal is to determine whether the observed frequency variations in the K -factor are a result of the estimator's uncertainty due to the finite sample size (see Fig. 4), or if these variations reflect actual changes in the K -factor with frequency that are not accounted for by the fitted models. Since most points ($\gg 5\%$) fall outside the CI, it can be inferred there are variations of the actual K -factor in frequency not captured by the fitted models which are not due to the uncertainty of the K -factor estimator. Although not shown, this is also the case for the rest of the cases.

V. CONCLUSIONS

This work has proposed a practical method to use hybrid RC plus CATR OTA chambers to emulate Rician channels with controllable K -factors at mmWave. The focus has been on the lower FR2 bands (24.25 – 29.5 GHz). The main goal has been creating a reference Rician channel to characterize beamforming and directional antennas. Therefore, the channel emulation procedure has employed a RHA as a reference. We hope this will pave the way to cost-efficient OTA testing of directional mmWave devices in channels with different K -factors that emulate real use cases.

First, the measured data has been analyzed to ensure it is valid for the procedures conducted in the further analysis of the parameters of the Rician distribution, e.g., the K -factor, the average received power, as well as the powers of the deterministic and the random signal components. It was established that all measured samples were independent, and the average power was well above the noise floor, i.e., at least 13 dB on average. However, the SNR might not be sufficient, or, more generally, the systems' losses might be too high for some of the cases, depending on the testing instruments used, as well as the use case. For example, if one desires to test throughput at high SNRs or signal levels, only a subset of the configurations may be capable of providing such signal level, as they are right now. This is not unsolvable, e.g. amplifiers, lower losses cables, and/or a 2:1 splitter could be used, but this should be

taken care of if actual OTA measurements are performed in this system.

Second, a bootstrap AD GoF test was used to confirm that the measurement data most likely follows a Rician distribution in all cases while the Rayleigh distribution is a good model for low K -factors, i.e., $K \leq -7.6$ dB.

Third, it has been proven that a wide range of K -factors can be generated with the proposed measurement setups. Employing the 39 different considered configurations, the produced frequency averaged K -factors or $\langle K \rangle_{FS}$ could be varied from -9.2 dB to 40.8 dB, with a maximum increment of 5.1 dB, while the average increment was 1.3 dB.

Fourth, the parameters that characterize the Rician distribution most likely followed by the measurement data, K , Ω , P_s , and P_d were analyzed. From them, several relevant points could be identified: the back absorber is very effective in attenuating the power of the CATR signal that is not directly coupled with the RHA. It is needed to use the CATR signal co-polarized with the RHA, which results in high K -factors, to have the lowest system losses, achieving also higher frequency stability for the same $\langle K \rangle_{FS}$ compared to the cross-polarization cases. Ω , P_s , and P_d show an inverse relation with the frequency. K does not show a general direct or inverse relation with the frequency. The proposed models to fit to the measurement data can explain most of the frequency variability of P_s in all cases, of Ω in most cases, of P_d in some cases, failing to explain it for K . The frequency variability of K is also proven not to be explained just by the uncertainty of the used estimator due to finite sampling.

Future work may include a MIMO setup, since the cases of RC and CATR have been combined through a splitter/combiner. This might include the simultaneous use of the two available RC antennas, as well as the two CATR polarizations, which can be accessed via two different ports, allowing up to a 4 MIMO channel. On the other hand, one of the system's limitations, especially for the cases where low K -factors are generated, is the large loss that the signal suffers. Also, an uncertainty analysis of the measurements and their impact on other aspects of the study, such as the K -factor or the frequency variations of the K -factor can be useful. Moreover, frequency modeling of K , Ω , P_s , and P_d is acknowledged as relevant to better understand the system behavior. In addition, the reasons why the GoF test is not giving exactly the expected 95% PR for Rician distribution should be further investigated. Finally, a relevant limitation of the proposed setup is that it cannot achieve average K -factors below -9.2 dB, which limits the minimum uncertainty of classic RC measurements such as TRP. An approach that can extend the low K -factors further down is to investigate the possibility of mounting both the DUT and the CATR on a turntable to achieve additional stirring of the cavity modes. This, in turn, would require an assessment of whether or not 600 samples would be enough to estimate lower K -factors or even if using another estimator might be a better option for such cases.

REFERENCES

- [1] 3GPP Technical Specification Group Radio Access Network. Technical

- report TR 38.827 V16.8.0, "Study on radiated metrics and test methodology for the verification of multi-antenna reception performance of NR User Equipment (UE); (Release 16)." Sept 2022.
- [2] 5GAA. (2021, Aug) Vehicular Antenna Test Methodology. [Online]. Available: https://5gaa.org/content/uploads/2021/08/5GAA_TR_Vehicular_Antenna_Test_Methodology.pdf
 - [3] P. Zhang, X. Yang, J. Chen, and Y. Huang, "A survey of testing for 5G: Solutions, opportunities, and challenges," *China Communications*, vol. 16, no. 1, pp. 69–85, 2019.
 - [4] A. Paulraj, R. Nabar, and D. Gore, *Introduction to Space-Time Wireless Communication*. Cambridge, U.K.: Cambridge Univ. Press, 2003.
 - [5] S. O. Rice, "Mathematical analysis of random noise," *The Bell System Technical Journal*, vol. 23, no. 3, pp. 282–332, 1944.
 - [6] T. S. Rappaport, S. Sun, R. Mayzus, H. Zhao, Y. Azar, K. Wang, G. N. Wong, J. K. Schulz, M. Samimi, and F. Gutierrez, "Millimeter Wave Mobile Communications for 5G Cellular: It Will Work!" *IEEE Access*, vol. 1, pp. 335–349, 2013.
 - [7] C.-X. Wang, J. Bian, J. Sun, W. Zhang, and M. Zhang, "A Survey of 5G Channel Measurements and Models," *IEEE Communications Surveys & Tutorials*, vol. 20, no. 4, pp. 3142–3168, 2018.
 - [8] M. Andersson, A. Wolfgang, C. Orlenius, and J. Carlsson, "Measuring performance of 3GPP LTE terminals and small base stations in reverberation chambers," in *Long Term Evolution*. Auerbach Publications, 2016, pp. 427–472.
 - [9] P.-S. Kildal, A. A. Glazunov, J. Carlsson, and A. Majidzadeh, "Cost-effective measurement setups for testing wireless communication to vehicles in reverberation chambers and anechoic chambers," in *2014 IEEE Conference on Antenna Measurements & Applications (CAMA)*, 2014, pp. 1–4.
 - [10] P.-S. Kildal and J. Carlsson, "New approach to OTA testing: RIMP and pure-LOS reference environments & a hypothesis," in *2013 7th European Conference on Antennas and Propagation (EuCAP)*, 2013, pp. 315–318.
 - [11] J. Kvarnstrand, P. Svedjenäs, E. Silfverswärd, and H. Helmius, "Integrating LoS and RIMP Measurements in a Single Test Environment," in *2021 15th European Conference on Antennas and Propagation (EuCAP)*, 2021, pp. 1–5.
 - [12] A. A. Ruiz, S. Hosseinzadegan, J. Kvarnstrand, K. Arvidsson, and A. A. Glazunov, "K-factor Evaluation in a Hybrid Reverberation Chamber plus CATR OTA Testing Setup," in *2024 18th European Conference on Antennas and Propagation (EuCAP)*, 2024.
 - [13] C. M. J. Wang, K. A. Remley, A. T. Kirk, R. J. Pirkel, C. L. Holloway, D. F. Williams, and P. D. Hale, "Parameter Estimation and Uncertainty Evaluation in a Low Rician K-Factor Reverberation-Chamber Environment," *IEEE Transactions on Electromagnetic Compatibility*, vol. 56, no. 5, pp. 1002–1012, 2014.
 - [14] P.-S. Kildal, X. Chen, C. Orlenius, M. Franzen, and C. S. L. Patane, "Characterization of Reverberation Chambers for OTA Measurements of Wireless Devices: Physical Formulations of Channel Matrix and New Uncertainty Formula," *IEEE Transactions on Antennas and Propagation*, vol. 60, no. 8, pp. 3875–3891, 2012.
 - [15] X. Chen, P.-S. Kildal, and S.-H. Lai, "Estimation of Average Rician K-Factor and Average Mode Bandwidth in Loaded Reverberation Chamber," *IEEE Antennas and Wireless Propagation Letters*, vol. 10, pp. 1437–1440, 2011.
 - [16] M. Z. Mahfouz, R. Vogt-Ardatjew, A. B. J. Kokkeler, and A. A. Glazunov, "Measurement and Estimation Methodology for EMC and OTA Testing in the VIRC," *IEEE Transactions on Electromagnetic Compatibility*, vol. 65, no. 1, pp. 3–16, 2023.
 - [17] D. Senic, K. A. Remley, C.-M. J. Wang, D. F. Williams, C. L. Holloway, D. C. Ribeiro, and A. T. Kirk, "Estimating and Reducing Uncertainty in Reverberation-Chamber Characterization at Millimeter-Wave Frequencies," *IEEE Transactions on Antennas and Propagation*, vol. 64, no. 7, pp. 3130–3140, 2016.
 - [18] T. Jia, Y. Huang, Q. Xu, Q. Hua, and L. Chen, "Average Rician K-Factor Based Analytical Uncertainty Model for Total Radiated Power Measurement in a Reverberation Chamber," *IEEE Access*, vol. 8, pp. 198 078–198 090, 2020.
 - [19] A. A. Glazunov, S. Prasad, and P. Handel, "Experimental Characterization of the Propagation Channel Along a Very Large Virtual Array in a Reverberation Chamber," in *Progress In Electromagnetics Research B*, vol. 59, 2014, pp. 205–217.
 - [20] C. Lemoine, E. Amador, and P. Besnier, "On the K -Factor Estimation for Rician Channel Simulated in Reverberation Chamber," *IEEE Transactions on Antennas and Propagation*, vol. 59, no. 3, pp. 1003–1012, 2011.
 - [21] J. D. Sanchez-Heredia, J. F. Valenzuela-Valdes, A. M. Martinez-Gonzalez, and D. A. Sanchez-Hernandez, "Emulation of MIMO Rician-Fading Environments With Mode-Stirred Reverberation Chambers," *IEEE Transactions on Antennas and Propagation*, vol. 59, no. 2, pp. 654–660, 2011.
 - [22] A. De Leo, P. Russo, and V. Mariani Primiani, "Emulation of the Rician K-Factor of 5G Propagation in a Source Stirred Reverberation Chamber," *Electronics*, vol. 12, no. 1, p. 58, Dec. 2022.
 - [23] J.-H. Choi, S.-O. Park, T.-S. Yang, and J.-H. Byun, "Generation of Rayleigh/Rician Fading Channels With Variable RMS Delay by Changing Boundary Conditions of the Reverberation Chamber," *IEEE Antennas and Wireless Propagation Letters*, vol. 9, pp. 510–513, 2010.
 - [24] C. L. Holloway, D. A. Hill, J. M. Ladbury, P. F. Wilson, G. Koepke, and J. Coder, "On the Use of Reverberation Chambers to Simulate a Rician Radio Environment for the Testing of Wireless Devices," *IEEE Transactions on Antennas and Propagation*, vol. 54, no. 11, pp. 3167–3177, 2006.
 - [25] I. Ahmed, M. Davy, H. Prod'homme, P. Besnier, and P. del Hougne, "Over-the-Air Emulation of Electronically Adjustable Rician MIMO Channels in a Programmable-Metasurface-Stirred Reverberation Chamber," 2023.
 - [26] 3GPP. Technical report TR 37.941 V17.0, "Radio Frequency (RF) conformance testing background for radiated Base Station (BS) Requirements (Release 17)." Mar 2022.
 - [27] RF SPIN. (2022) DRH50 Datasheet. [Online]. Available: <https://www.rfspin.com/wp-content/uploads/2022/04/DRH50--RF-SPIN.pdf>
 - [28] CTIA, "01.73 Supporting Procedures." Nov 2023.
 - [29] Bluetest. (2020) 5G OTA DEVICE TESTING IN THE RTS65. [Online]. Available: https://www.bluetest.se/files/5G_RevA.pdf
 - [30] K. A. Remley, S. Catteau, A. Hussain, C. L. Nogueira, M. Kristoffersen, J. Kvarnstrand, B. Horrocks, J. Fridén, R. D. Horansky, and D. F. Williams, "Practical Correlation-Matrix Approaches for Standardized Testing of Wireless Devices in Reverberation Chambers," *IEEE Open Journal of Antennas and Propagation*, vol. 4, pp. 408–426, 2023.
 - [31] R. J. Pirkel, K. A. Remley, and C. S. L. Patane, "Reverberation Chamber Measurement Correlation," *IEEE Transactions on Electromagnetic Compatibility*, vol. 54, no. 3, pp. 533–545, 2012.
 - [32] International Electrotechnical Commission, Electromagnetic Compatibility (EMC)–Part 4–21, "Testing and Measurement Techniques–Reverberation Chamber Test Methods, Standard IEC 61000–4–21," Jan 2011.
 - [33] C. M. J. Wang, K. A. Remley, A. T. Kirk, R. J. Pirkel, C. L. Holloway, D. F. Williams, and P. D. Hale, "Parameter Estimation and Uncertainty Evaluation in a Low Rician K-Factor Reverberation-Chamber Environment," *IEEE Transactions on Electromagnetic Compatibility*, vol. 56, no. 5, pp. 1002–1012, 2014.
 - [34] W. Rolke and C. Gutierrez Gongora, "A chi-square goodness-of-fit test for continuous distributions against a known alternative," *Computational Statistics*, vol. 36, no. 3, pp. 1885–1900, May 2021.
 - [35] C. Lemoine, P. Besnier, and M. Drissi, "Investigation of Reverberation Chamber Measurements Through High-Power Goodness-of-Fit Tests," *IEEE Transactions on Electromagnetic Compatibility*, vol. 49, no. 4, pp. 745–755, 2007.
 - [36] M. Stephens, "EDF Statistics for Goodness of Fit and Some Comparisons," *Journal of the American Statistical Association*, vol. 69, no. 347, pp. 730–737, 1974.
 - [37] M.A. Stephens, "Bootstrap Based Goodness-Of-Fit-Tests," *Metrika*, vol. 40, pp. 243–256, 1993.
 - [38] D. Hill, M. Ma, A. Ondrejka, B. Riddle, M. Crawford, and R. Johnk, "Aperture excitation of electrically large, lossy cavities," *IEEE Transactions on Electromagnetic Compatibility*, vol. 36, no. 3, pp. 169–178, 1994.